1 The rate of sedimentation from turbulent suspension: an experimental model with application

2 to pyroclastic density currents and discussion on the grain-size dependence of flow runout

3 P. Dellino^{1*}, F. Dioguardi², D.M. Doronzo³ and D. Mele⁴

¹ Dipartimento di Scienze della Terra e Geoambientali, Università di Bari, Italy; ² British Geological
Survey, The Lyell Centre, Edinburgh, United Kingdom; ³ Institute of Earth Sciences "Jaume
Almera" – CSIC, Barcelona, Spain; ⁴Sezione di Napoli Osservatorio Vesuviano - Istituto Nazionale
di Geofisica e Vulcanologia, via Diocleziano 328, 80124 Naples, Italy.

- 8
- 9 Abstract

10 Large-scale experiments generating ground-hugging multiphase flows were carried out with the aim of modelling the rate of sedimentation S_r of pyroclastic density currents. The current was initiated by 11 12 the impact on the ground of a dense gas-particle fountain issuing from a vertical conduit. On impact, 13 a thick massive deposit was formed. The grain size of the massive deposit is almost identical to that of the mixture feeding the fountain, suggesting that similar layers formed at the impact of a natural 14 15 volcanic fountain should be representative of the parent grain-size distribution of the eruption. The 16 flow evolved laterally into a turbulent suspension current that sedimented a thin, tractive layer. A 17 good correlation was found between the ratio transported/sedimented load and the normalized Rouse number P_n^* of the turbulent current. A model of the sedimentation rate was developed, which shows 18 19 a relationship between grain size and flow runout. A current fed with coarser particles have a higher 20 sedimentation rate, a larger grain-size selectivity and runs shorter than a current fed with finer particles. Application of the model to pyroclastic deposits of Vesuvius and Campi Flegrei of Southern 21 22 Italy resulted in sedimentation rates falling inside the range of experiments and allowed defining the duration of pyroclastic density currents τ_{dep} , which add important information on the hazard of such 23 24 dangerous flows. The model could be possibly extended, in the future, to other Geological density 25 currents as, for example, turbidity currents.

26

28

27 Keywords: Pyroclastic density currents, sedimentation rate, turbulent suspension, experiments

^{*}Corresponding author: pierfrancesco.dellino@uniba.it

30 1. Introduction

31 The formation of sedimentary deposits is in many cases regulated by the passage of turbulent currents 32 carrying a substantial particle load. Common examples are rivers, turbidity currents and pyroclastic density currents (Gladstone et al., 1998; Kneller and Buckee, 2000). The flow carries solid particles 33 34 by three main modes (Rouse, 1939; Middleton and Southard, 1984): bedload, suspension and wash 35 load. Bedload concerns the material moved by traction on the ground; wash load concerns particles 36 so fine that are intimately coupled to fluid turbulence and are carried away by the current. Suspension 37 refers to particles that are sustained by fluid turbulence and settle when their terminal velocity is 38 lower than the current shear velocity. The suspension load is thought to represent about 90-95% of 39 the total particulate material in the current. It is the rate of sedimentation from turbulent suspension 40 that feeds the sediment layer, allows aggradation of deposit thickness and regulates the current runout. 41 In the time-space evolution of a flow, particles, after transportation in suspension, eventually settle 42 to the ground and form the bedload that, upon some tractional movement, comes to rest and forms 43 the final deposit (Branney and Kokelaar, 2002; Sulpizio and Dellino, 2008; Sulpizio et al., 2014; 44 Dufek, 2016). The structural configuration of the layer is acquired by the last movement of the 45 sediment in the bedload, which leads to the formation of asymmetrical structures such as ripples, sand 46 waves and cross lamination.

47 The flow of pyroclastic density currents moves in contact with the ground due to its higher density 48 with respect to the surrounding atmosphere. The loss of particles from sedimentation, combined with 49 fluid entrainment from the atmosphere, results in a reduction of concentration, with a consequent 50 lowering of fluid density. It is related to the fact that the flow is composed of gas and particles and behaves as a "pseudofluid" which density is given by $\rho_f = \rho_s C + \rho_g (C - 1)$, where ρ_s is particle 51 density, ρ_f is fluid density, ρ_g is gas density and C is particle volumetric concentration (all symbols 52 53 are defined in Table 1). It is known that pyroclastic density currents, as results from the density 54 reduction due to sedimentation, at some point stop moving laterally and start lofting from the ground 55 in the form of a buoyant phoenix cloud (Neri and Macedonio, 1996; Sparks et al., 1997; Branney and

Kokelaar, 2002; Andrews and Manga, 2011, 2012), aided by buoyancy resulting from entrainment
and thermal expansion of atmosphere.

The ability of a turbulent current to transport a particle in suspension is a function of the particle Rouse number $P_n = w_t/ku_*$ (Rouse, 1939), where u_* is the current shear velocity, which is related to the turbulent shear stress (Pope, 2000; Schlichting and Gersten, 2000), *k* is Von Karman constant = 0.4 and w_t is particle terminal velocity

62
$$w_t = \sqrt{\frac{4Dg(\rho_s - \rho_f)}{3C_d \rho_f}} (1)$$

63 where *D* is particle size, *g* is gravity acceleration, C_d is particle drag coefficient. Particles with P_n 64 lower than 2.5 are carried in suspension by turbulence, meaning that they are suspended until u^* 65 doesn't drop to values lower than w_t (Middleton and Southard, 1984; Valentine, 1987; Branney and 66 Kokelaar, 2002; Dellino et al., 2008).

Equation (1) gives a good estimation of particle settling velocity if particle volumetric concentration does not exceed a few percent, which is the case of the suspension currents considered in this paper. The particle volumetric concentration (hence density) is stratified within the current. The maximum volumetric concentration of particles that can be transported in suspension, i.e. the maximum current capacity, is a function of the Rouse number of the particulate mixture taken in suspension P_{nsusp} . It is regulated by the Rouse concentration profile over current height y

73
$$C_{tot} = C_0 \frac{1}{H_T - y_0} \int_{y_0}^{H_T} \left(\frac{H_T - y_0}{y_0} \frac{y}{H_T - y} \right)^{P_{nsusp}} dy$$
 (2)

where C_{tot} is the total concentration of the current, H_T is current total thickness and C_0 is a value of known concentration at a specific height y_0 , which is assumed to be the value of concentration at maximum packing in contact with the ground (0.75 in this paper). From (2) it can be inferred that a current carrying a finer mixture (lower P_{nsusp}) can transport, at maximum capacity, a higher concentration than one having the same shear velocity, but carrying coarser particles (higher P_{nsusp}). The solid load constituting a suspension current, especially in the case of pyroclastic density currents, is made up of a mixture of different components (lithics, glassy fragments and crystals) with different

size, density and shape, thus different terminal velocity. The Rouse number of the solid material in
the current must be expressed as the average of the particulate mixture,

83
$$P_{n_{avg}} = \sum_{i=1}^{n} P_{ni} C_i / C_{tot}$$
 (3)

84 with the subscript *i* referring to the *i*_{th} particle-size class and *n* being the number of size classes.

The ratio between $P_{n_{avg}}$ of the material in the current and P_{nsusp} is here defined as the normalized Rouse number P_n^* of the current. When it is higher than 1, a current has a particle volumetric concentration in excess of its maximum capacity, e.g. it is over-saturated of particles, which favours sedimentation. When it is lower than 1, a current has a particle volumetric concentration lower than its maximum capacity, e.g. it is under-saturated, and could potentially include additional sediment that is being eroded from the substrate. Very coarse particles, namely those with P_n higher than 5, settle from suspension without being much influenced in their trajectory by turbulence.

92 Particles in a pyroclastic density current often come from the fountaining of an eruption column and 93 generally are over-saturated with particles. In fact, pyroclastic density currents leave continuous 94 deposits on the ground, meaning that during most of the runout they are in sedimentation mode. The sedimentation rate $S_r = w_t \rho_s \gamma$ is a measure of the mass of particles sedimenting with time per unit 95 96 area, where γ is the proportion of particles settling from suspension. It is convenient to express the sedimentation rate by means of the sum of the contribution of each size class in the mixture S_r = 97 $\sum_{i=1}^{n} S_{ri}$ where $S_{ri} = w_{ti} \rho_{si} \gamma_i$, where S_{ri} is the sedimentation rate of the ith size class, w_{ti} is the 98 99 terminal velocity of the ith size class, ρ_{si} is the density of the ith size class and γ_i is the proportion of 100 particles of the ith size class settling from suspension.

101 The grain-size distribution of a deposit is generally represented by a histogram expressed in ϕ units 102 $\phi = -\log_2 d$, with *d* particle diameter in millimetres. It represents the distribution of the weight 103 fraction ϕ_i of each size class in the deposit, with $\sum_{i=1}^{n} \phi_i$ summing to 1 (or 100%). In the case of 104 deposits formed by sedimentation from turbulent suspension, it is here assumed that the grain-size 105 distribution represents also the proportion of the sedimentation rate of each size class. Thanks to this 106 assumption, the values of γ_i can be easily calculated once the total sedimentation rate S_r , the terminal 107 velocity w_{ti} and density of each size class ρ_{si} are known.

108 The growth of deposit thickness with time at a location, i.e. the layer aggradation rate, is given by $A_r = S_r / \rho_{dep}$ where A_r is the aggradation rate and ρ_{dep} is deposit density, measured in the field as 109 0.6 $\rho_{\rm s}$ in this study. Depositional time $\tau_{\rm dep}$ is given by $\tau_{dep} = \frac{H_{dep}}{A_r}$ where H_{dep} is deposit thickness. 110 111 If deposit density and thickness are measured in the field, and the rate of sedimentation can be 112 modelled, it is possible to reconstruct the depositional time, which to a good approximation represents 113 the time it took for the current to pass that particular location. The depositional time is an important 114 indicator of the potential impact that a pyroclastic density current can have on human health, since it 115 quantifies the residence time of hot volcanic ash that can be inhaled by people potentially exposed to 116 these dangerous flows (Horwell and Baxter, 2006). Even a very low volumetric concentration of ash 117 in suspension is unbreathable, and is one of the main causes of mortality of pyroclastic density 118 currents. A model of the sedimentation rate from suspension could greatly help assessing the hazard 119 of pyroclastic density currents. Unfortunately, up to now, no such model exists. In fact, in the 120 computational fluid dynamic simulations of pyroclastic density currents, the effect of sedimentation 121 is generally not included.

This paper describes experiments carried out for developing a model of the sedimentation rate based on data derived from deposits. The model highlights the grain-size dependence of flow runout. Application to natural deposits leads to calculation of the depositional time of natural currents, which helps assessing the hazard to human health.

126

127 2. Experiments and laboratory investigation

The experiments were carried out with the apparatus described in detail in Dellino et al., 2007; 2010a; and 2010b, which allowed the reproduction of various regimes of explosive eruptions (Dellino et al., 2014). In this paper, only the results of experiments generating substantial density currents are considered (Dellino et al., 2010b). The particulate material used in the experiments comes from deposits of Vesuvius and Campi Flegrei volcanoes in Southern Italy, and covers an ample range of size, density and particle shape. For each run, up to 350 kg of particles were used. The grain size of two compositions, representing the coarse (from Vesuvius) and fine (from Campi Flegrei) end members, are shown on fig.1. The coarser composition, ranging from lapilli to fine ash (fig. 1a), is made of dense lithic, vesicular glass and crystal components, while the finer one, mostly fine ash (fig. 1b), is made almost exclusively of glass fragments.

138 Experiments were carried out at various temperatures, from ambient up to 300 °C. The effect of high temperature was that of reducing the density of the carrier fluid and forming a buoyant phoenix cloud 139 140 at the end of runout (Dellino et al., 2010b). Additional details that emerged, by the experiments, on 141 the effect of temperature on various regimes are deferred to Dellino et al. (2014). The experimental 142 design (fig. 2) consists of 2 interconnected packs of 16 pressurized-gas bottles (the gas storage 143 compartment); a high-pressure section consisting of 18 steel-reinforced rubber hoses each 30 m long; 144 a rapid-compression section consisting of 18 steel-reinforced rubber hoses each 1.5 m long; and a 145 low-pressure section consisting of a 3.2-m-long stainless-steel conduit with a 0.6-m internal diameter, 146 mounted on a massive base plate. The gas bottles are coupled to the high-pressure section via two 147 valves and a hub, in line with manometers that control the reservoir pressure and the pressure in the 148 high-pressure section. High-speed solenoid valves connect the high-pressure section via a second hub 149 to the rapid compression section. The short hoses are connected to eighteen blow nozzles in the base 150 plate of the low-pressure section. The pyroclastic material is placed into the conduit and rests directly 151 on the base plate. The experiment starts by opening the valves that connect the gas-storage 152 compartment to the high-pressure section until the desired pressure is reached in the 30 m long hoses. 153 The computer controlled opening of the solenoid valves connects the high-pressure section to the 154 low-pressure section (via the rapid compression section) and allows a fast coupling of the pressurized 155 gas with the pyroclastic material filling the conduit, which while mixing with the expanding gas, 156 accelerates along the conduit. The two-phase mixture is finally expelled from the conduit in the form 157 of a dense gas-particle fountain, reaching a maximum height over 10 m (fig. 3a). On hitting the 158 ground, the fountain resembled the collapse of an eruptive column similar to that generating a natural 159 pyroclastic density current.

160 Upon the impact of the fountain on the ground (fig. 3b), the normal stress of the fluid was transformed 161 into tangential stress, which led to a flow that evolved laterally into a fully turbulent, gas-particle 162 shear current, a few meters thick, moving at several m/s (fig. 3c). Deposits of measurable thickness 163 (at least a few millimetres) formed on the ground upon the passage of the current. At the impact zone, 164 where the lateral flow was not fully developed yet, a tens of centimetres thick, massive deposit, was 165 formed (fig. 3d). It represents the excess of solid material that could not be transported into the lateral 166 flow, and was emplaced "en masse" (Sulpizio et al., 2014; Roche, 2015). It is important to note that 167 the grain-size distribution of the massive layer is very similar to that of the original particle load in 168 the conduit. This happens both with the coarse and fine particle mixtures used in the experiments (fig. 169 4a and b). It reveals that there is not an effective grain-size selection between the particulate mixture 170 issuing from the conduit and the material emplaced en masse at the impact on the ground. It means 171 that the grain size of massive layers formed by similar collapses of dense volcanic fountains should 172 be considered as representative of the parent particle population of natural eruptions. This deposit 173 facies, which resembles a massive pyroclastic flow (Branney and Kokelaar, 2002), makes transition, 174 laterally, into a thin structured layer, similarly to what is observed and documented in certain 175 ignimbrites (Brown and Branney, 2013). The thin layer shows sedimentary structures such as ripples 176 (fig. 3e), which are characterized by an asymmetrical distribution of particles. The finer load occurs 177 at the foreset and the coarser load at the backset, suggesting a selective transportation of the bedload, 178 which is typical of tractive processes occurring at the base of natural currents. These features are 179 common among deposits formed by pyroclastic density currents, with the difference that natural 180 layers have a much higher thickness and represent the aggradation of multiple tractional structures 181 formed during the time integrated passage of the flow, which is much longer than that of experiments. 182 The deposit thins out with increasing distance from the impact zone and has a fan shaped distribution

covering, with a thickness ranging from a few millimetres to a few centimeters, an area of up to about 2000 m² (fig. 3f). The shear current was continuously fed from the fountain for several seconds. In that time period the deposit was formed by steady sedimentation of particles from suspension, and final bedload traction. When the fountain stopped feeding the current, the flow rapidly decelerated and only the finest particulate material of the upper part of the current continued moving as a wash load, for a long time (Supporting video). The wash load was spread well over the deposit fan-shaped area and formed a very thin, submillimetric, veil of ash.

190 The current runout was recorded by a network of pressure sensors and multiple high-definition digital 191 video cameras (Dellino et al., 2007, 2010a, 2010b, 2014). For each experiment, thickness and speed 192 of the current were recorded at multiple stations along runout, starting from the impact point and up 193 to about 20 m of distance. The distance between successive stations was set at 1 m for runs spreading 194 on a smaller area and at 2 meters for larger ones. Sediment samples were collected from each station. 195 Sampling was done by collecting the sediment from a rectangular area on the ground, about 1 m^2 , 196 which allowed calculation of the mass per unit area of sediment deposited at each station. A total of 197 18 samples representing the total number of locations out of 6 experimental runs is considered in this 198 paper, on which grain-size, density and particle shape analyses were carried on.

For each of the 18 locations, by combining the processing of sensors and video camera recordingsand laboratory analyses of the sediment samples, the following parameters were obtained:

• the shear velocity of the current u_* ;

• the particle volumetric concentration of each size class C_i and the total particle volumetric 203 concentration C_{tot} ;

- the Rouse number of each size class P_{ni} and the average Rouse number $P_{n_{ava}}$;
- the Rouse number at maximum suspension capacity P_{nsusp} and the normalized Rouse number 206 P_n^* ;
- the proportion of particles of each size settling from suspension γ_i ;

• the rate of sedimentation of each size class S_{ri} and the total sedimentation rate S_r ;

- the settling velocity of each size class *w*_{ti};
- the density of each size class ρ_{si} ;
- the flow density ρ_f ;
- the multicomponent grain-size distribution including the shape of particles;
- 213
- the particle mass flow rate PMFR.

214 In particular, the particulate mass flow rate at the impact zone was measured as the product of the 215 area of impact, velocity of impact and density of the flow. The PMFR of each size class in the current 216 was calculated, at each station, by subtracting the total mass of sediment deposited at all previous 217 stations from the particulate mass flow rate at the impact, and using as the area crossed by the flow, 218 the value measured by image analysis upon flow front passing from each station. The current density 219 due to the particle load of each size class was calculated by dividing the mass flow rate of each size 220 class by the average velocity of the current. The total mass and grain-size distribution of each 221 component in the particulate mixture was measured in the laboratory before each run, as it was done 222 also for the samples taken at each station. The mass of material transported in the current at successive 223 stations was calculated by subtracting the mass of sediment deposited at previous stations from the 224 total mass. The particle volumetric concentration of each size class of the current C_i was calculated 225 by dividing the bulk density of the current by the particle density of each size class. The total 226 sedimentation rate was calculated at each station by the mass of sediment per unit area divided by the 227 time of sedimentation. The time of sedimentation was measured at each station starting from the 228 arrival of the flow front and ending by the passage of the wash load. The total sedimentation rate was 229 partitioned among size fractions according to the partitioning of the grain-size distribution. The 230 proportion of particles settling from suspension γ_i of each size class was calculated by dividing the 231 sedimentation rate of each size class by the settling velocity and particle density. For more details on 232 the experimental methods, techniques and uncertainties, see the Supporting file A. The experiments 233 covered an ample range of flow parameters. In particular, the sedimentation rate S_r was between 0.009

/ 1.17 kgm⁻²s. It is in the same order of magnitude of the sedimentation rate obtained by means of
 lagrangian multiphase numerical simulations (Valentine et al., 2011; Doronzo et al., 2017). For the
 range of other experimental parameters see the summary Table 2.

237

3. The experimental model

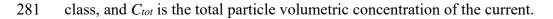
239 The ratio between the particle volumetric concentration of each size class C_i and the proportion of particles of each size class settling from suspension γ_i of each experiment is well correlated with the 240 241 Rouse number of each size class P_{ni} , as it should be expected in a turbulent suspension current where 242 the attitude of particles to be transported (or sedimented) is a function of the balance between terminal 243 velocity and shear velocity. On fig. 5, the different slopes in the regression equation of a current 244 carrying coarser particles compared with one carrying finer ones demonstrates that flows having a 245 different normalized Rouse number P_n^* have also a different attitude toward sedimentation (or 246 transportation), which depends on the excess of particle load (oversaturation) with respect to 247 maximum current capacity. To take into account this factor, the ratio C_i/γ_i of all particle sizes and components of all samples was plotted against P_{ni}/P_n^* . The equation of the regression line: 248

249
$$\frac{C_i}{\gamma_i} = \frac{P_{n_i}}{P_n^*} 10.065 + 0.1579 (4)$$

250 well approximates data of all experiments (fig. 6).

251 The regression line of equation (4) can be used either to predict the proportion of each size class of particles settling from suspension γ_i if the Rouse number of each size class P_{ni} , the normalized Rouse 252 253 number P_n^* and the particle volumetric concentration of each size class C_i are known or to obtain C_i if P_{ni} , P_n^* and γ_i are known. Unfortunately, it is difficult to estimate the values of C_i or γ_i of natural 254 255 pyroclastic density currents. The particle parent population that issues from the volcanic conduit and feeds pyroclastic density currents is generally unknown. In fact, there is a strong geological evidence 256 257 that it changes from volcano to volcano and from eruption to eruption, depending mostly on magma 258 fragmentation processes. It is to expect that the relative proportions of the size fractions in the

259 transported material should be different from the proportions of the material settling on the ground. 260 In fact, the grain-size distribution will evolve as particles selectively sediment as a function of grain 261 size and density. While it is reasonable to hypothesize a substantial grain-size difference, along 262 runout, between the material transported at a certain location and the material deposited far away, the 263 difference between the grain size transported at some point and that deposited at the same point should 264 be smaller. Following this line, we tested whether the difference in grain size between the sediment 265 sampled at a station and that of the particulate mixture transported in the current at the same station was small enough as to permit the use of the sediment size as a "first guess" of the transported material 266 in equation (4) for reconstructing the sedimentation rate of the experiments. The relative proportions 267 268 of the size fractions in the transported material at a station were obtained, as described in the previous 269 paragraph, by subtracting the total mass of sediment deposited at all previous stations from the total 270 mass. We made the test by using a goodness-of-fit formula based on the chi-square statistics: 100% - $\left(\sum_{i=1}^{n} \left(\frac{O_i - E_i}{E_i}\right)^2\right)$. O_i is the weight % of the transported material of the i_{th} size class (Observed value 271 in Statistics), E_i is the weight % of the deposited material of the i_{th} size class (Expected value in 272 273 Statistics). The components were summed together as to obtain, for each class, a weight not smaller 274 than 5%, as it is suggested in Statistics when using percent data in the chi-square test (Davis, 2002). 275 We obtained a fitting typically better than 90% (see Supporting file C and D for examples), which ensures that the grain-size distribution of the deposit can be used as a "first guess" of the grain-size 276 277 distribution of the transported material, without too much error. The concentration of each component of each size class of the transported material was, then, reconstructed by means of the grain-size 278 distribution of the deposit at each station by $c_{trans_i} = \frac{\phi_i / \rho_{s_i}}{\sum_{i=1}^n \phi_i / \rho_{s_i}} * C_{tot}$, where c_{trans_i} is the particle 279 volumetric concentration of the i_{th} size class, $\frac{\phi_i/\rho_{s_i}}{\sum_{i=1}^n \phi_i/\rho_{s_i}}$ is the volume fraction occupied by the i_{th} size 280



By means of the values of
$$c_{trans_i}$$
, and rearranging equation (4), the contribution of each particle
size of each component in the sedimentation rate $\gamma_{proxy_i} = \frac{c_{trans_i}}{\left(\left(10.065*P_{n_i}/P_n^*\right)+0.1579\right)}$ was obtained.

By means of γ_{proxy_i} , and using the values of settling velocity and particle density of each size 284 285 class, the sedimentation rates were calculated and compared with the experimental values. The plot 286 on fig. 7 shows the regression line approximating data points. Judging from the correlation 287 coefficient, while some scatter is visible, the fitting is good. The slope of the regression line is, 288 however, a little smaller than 1, suggesting that the calculated values are a little underestimated with 289 respect to the experimental ones, which can be attributed to the approximation that was made by 290 using the grain-size distribution of the deposit as a "first guess" of the grain-size distribution of the 291 transported material. The underestimation suggests that the grain size of the sediment must be a 292 little coarser than that of the transported material, as it is expected from a current that settles, 293 selectively, more of the coarser than of the finer particle load. We looked for correcting the underestimation and found the grain-size shift necessary to adjust the γ_{proxy_i} values. Details of the 294 295 method are shown in the Supporting file B. By means of the application of the grain-size shift, the corrected proportions of the sedimentation rate of each size class are recalculated as: $\gamma_{true_i} =$ 296 $\gamma_{proxy_i} * 0.7 + \gamma_{proxy_{i+1}} * 0.3$, where γ_{true_i} is the correct value. 297

By means of the values of γ_{true_i} the sedimentation rates were recalculated and compared with the experimental ones, resulting in the regression of fig. 8, by which the final model equation of the sedimentation rate is obtained

301
$$S_r = \left(\sum_{i}^{n} \rho_{s_i} w_{t_i} \left(\frac{c_{trans_i}}{\left(\left(10.065 * P_{n_i}^* \right) + 0.1579 \right)} * 0,7 + \gamma_{poxy_{i+1}} * 0.3 \right) \right) - 0,01 (5)$$

302 By means of equation (5), the final fitting of fig. 9 is obtained, which shows, to a good

303 approximation, a 1 to 1 ratio between measured and calculated sedimentation rates.

By rearranging terms, it is also possible to reconstruct the particle volumetric concentration of each
 size and component transported in the current, starting from the proportion in the deposit, by

306
$$c_{trans_{true_i}} = (\gamma_{proxy_i} * 0.7) + (\gamma_{poxy_{i+1}} * 0.3)) * ((10.065P_{n_i}^*) + 0.1579) (6)$$

307 where $c_{transtrue_i}$ is the corrected concentration of the i_{th} size class in the current. By normalizing to 308 1 the sum of the values of $c_{transtrue_i}$ of all the size classes, the grain-size distribution of the particle 309 mixture in the current is calculated.

310 On fig. 10, examples of the comparison between the grain-size distribution of the transported material 311 and that of the sediment material are shown. The sediment particulate mixture is a little bit coarser 312 than the particle load transported in the current, as it is expected in a current that settles selectively 313 more of the coarser than of the finer particle load. This happens when the coarse composition of 314 Vesuvius is used in experiments (fig. 10a), where the weight % of the coarser size classes is constantly 315 higher in the sedimented than in the transported material down to a size of 3ϕ , then the behaviour is 316 inverted for the finest class sizes. The difference is less obvious when the particulate mixture is composed of fine material (fig. 10b), as observed in the experiment with the composition of Campi 317 318 Flegrei. In this case, in fact, the weight % of the coarser size classes is higher in the transported 319 material down to 2.5 ϕ , then it is higher in the sedimented material from 2.5 and 5 ϕ , and finally it is 320 again higher in the transported material, indicating a lack of a particular selectivity of grain size. An 321 additional proof of the difference in selectivity between "coarse" and "fine" currents is shown on 322 Fig.11 where a comparison between the grain-size evolution of deposits as a function of distance 323 from the impact zone is shown for two experiments. In the "coarse" run a small but significant 324 variation of grain size as a function of increasing distance is noticeable, while for the "fine" run the 325 grain size is more or less the same at various distance. While the experiments do not represent the 326 real scale of distance travelled by natural currents, the clear difference between currents carrying 327 coarser vs fine pyroclasts suggests that pyroclastic density currents transporting mostly fine ash should show less grain-size variations along runout. The comparison of the sedimentation rate at two 328 329 locations, which represent experiments fed with the coarse and fine end members, reveals some 330 additional aspects of the grain-size dependence of runout of pyroclastic density currents. The relative

331 data sets are included in the Excel worksheets of the Supporting file C and D for a detail analysis. 332 Here we just discuss the fundamental results. While the flow characteristics, i.e. current velocity, are 333 not much different, a big difference, between the coarse and fine cases, is in the ratio between the 334 particle mass flow rate and the sedimentation rate. It is much smaller in the case of the experiment with the coarser material compared to the finer one (four times smaller, see Supporting file C and D). 335 336 The coarser current has a much higher sedimentation rate than the finer one (tens of times, see 337 Supporting file C and D). Summing up, finer currents can suspend a higher amount of particles 338 (because of the lower Pn), emplace less material along runout, maintain a significant density difference with respect to the atmosphere, hence a higher mobility and a longer runout compared to 339 340 coarser currents. As a consequence, fine pyroclastic density currents can run faster, longer and leave 341 thin, widely spread deposits. This conclusion seems to be corroborated by the fact that some of the 342 most widespread historical pyroclastic density currents known up to date, for example the 1.8 ka 343 Taupo ignimbrite of New Zealand (Wilson et al., 1995; Dade and Huppert, 1996; Manville et al., 344 2009), show thin, fine-grained deposits, which grain size doesn't change much with travel distance.

345

4. Model application to natural pyroclastic deposits and scaling to experiments

The experimental model developed in this paper was applied to the deposits of pyroclastic density 347 348 currents of the Mercato Plinian eruption at Vesuvius and of the Agnano Monte Spina Plinian eruption 349 of Campi Flegrei in Southern Italy. Details on the eruptions and stratigraphy of deposits can be found 350 in de Vita et al., 1999; Dellino et al., 2004; Mele et al., 2011, 2015. The layers considered in the 351 present study were formed by the passage of density currents fed by the collapse of an eruption 352 column and show, at the localities sampled in this study, a facies characterized by tractional structures 353 (fig. 12a) and inclined lamination (fig. 12b), suggesting that transportation and sedimentation were 354 from flows carrying a particulate load by turbulent suspension, and final tractional movement at the 355 bedload.

The layers are 0.5 and 0.2 m thick for Mercato and Agnano Monte Spina, respectively. Deposit density is 1476 and 1295 kg/m³ for Mercato and Agnano Monte Spina, respectively. They are composed of vesicular glass, dense lithics and crystals, which multicomponent grain size is shown on fig. 13 a and b, respectively. The density, shape and settling velocity of each size class of each component of the deposits were calculated using the same techniques of the experimental samples.

361 The flow parameters needed for the application of our sedimentation rate model were calculated by 362 means of the software Pyflow (Dioguardi and Dellino, 2014), which is based on the models of Dellino 363 et al. (2008) and Dioguardi and Mele (2015). The calculation used in the present paper utilizes the 364 concept of hydraulic equivalence. If two components with different median size, density and shape, 365 settle together, they are hydraulically equivalent and have the same settling velocity. By this 366 assumption, the software equates the settling velocity of the two components and solves for the 367 current shear velocity u_* , total concentration over flow height C_{tot} and Rouse number at maximum 368 suspension capacity Pn_{susp} . The software finds a range of solutions that considers the variation of 369 deposit particle characteristics. For the sake of simplicity, we restrict our analysis to the average 370 solution, and give the uncertainty in terms of \pm one standard deviation around the average.

By combining the particles data and flow parameters obtained by the software Pyflow: C_i , P_{ni} , P_{navg} 371 372 and P_n^* were calculated, and by means of the combined use of eq. (4), (5) and (6) the sedimentation 373 rate was obtained. In the Supporting file E and F, an Excel worksheet contains all the input data and 374 results of the average solution, as to allow following step by step the calculations. The sedimentation rate is about $0.59^{+0.19}_{-0.22}$ and $0.38^{+.08}_{-.17}$ kg/m²s for Mercato and Agnano Monte Spina, respectively. It 375 376 falls inside the range of experiments, suggesting that the application of the model to natural deposits 377 doesn't imply an unwarranted extrapolation of results outside the experimental range. By comparing 378 data of file E and F and table 2 it is possible to judge how other important parameters scale between 379 experiments and natural pyroclastic density currents. The shear velocity of the Mercato and Agnano 380 Monte Spina pyroclastic density currents, while in the same order of magnitude of experiments, is 381 about threefold. The thickness of natural currents is much larger than that of the experiments.

382 Combining shear velocity and flow thickness and recalling that the velocity profile is a function of the shear velocity (see Supporting material A), it results that natural currents typically reach, with 383 384 increasing height, a speed of tens of m/s, while in the experiments the maximum speed was a little 385 bit lower than 10 m/s. The grain size of natural deposits is in the same range of experiments as it is also the particle volumetric concentration and the normalized Rouse number, P_n^* . Summing up, while 386 387 velocity and thickness of natural currents are larger than experiments, the experiments well preserve 388 the scale of natural flows in their basal part, where sedimentation occurs, justifying the fact that the 389 sedimentation rate of natural deposits is well inside the range of experiments. The tractional features 390 of natural deposits are similar to the experimental ones, whereas the thickness of deposits is much 391 larger in the natural case. Since the growth of deposit thickness with time is a function of the 392 aggradation of the material sedimented from turbulent suspension, the larger thickness of natural 393 deposits means a longer duration of the passage of natural pyroclastic density currents with respect 394 to the experiments. For approximating the duration of the passage of the natural currents, first the aggradation rate A_r and finally the deposition time τ_{dep} were calculated, by recalling the definition 395 given in the introduction section. A_r is $4^{+1.3}_{-1.5} \times 10^{-4}$ and $2.9^{+.07}_{-.13} \times 10^{-4}$ m/s for Mercato and Agnano 396 Monte Spina, respectively, and τ_{dep} is 1240^{+765}_{-307} and 681^{+554}_{-125} s. It means that the passage of the 397 398 currents, at the location where the deposits were sampled, lasted around 20 minutes in the case of 399 Mercato and around 11 minutes in the case of Agnano Monte Spina. This is consistent with the 400 observation of historical eruptions, where the flow lasted for several minutes to hours (e.g. Lube et 401 al., 2007). During that time period the territory was engulfed with thick, expanded, fast and hazardous 402 currents, loaded with unbreathable hot ash (Horwell and Baxter, 2006). It is important to take note of 403 such information, when projecting for emergency plans and risk-reduction measures.

404

405 **5. Discussion and future perspective**

406 By means of large-scale experiments, a novel model of the sedimentation rate from turbulent 407 suspension (Equation 5) was obtained. The sedimentation rate strongly influences the runout of

408 pyroclastic density currents, depending on the grain-size of the particulate mixture. If the grain size 409 of the current is coarser (coarse ash to lapilli), the flow sediments selectively the particulate load, 410 making the particle mixture gradually finer along the runout. When, instead, the particulate mixture 411 is finer (fine ash) there is less selective transportation, hence deposition. In this case, particles have a 412 smaller Rouse number, which is the exponent of the concentration profile, resulting in an almost 413 evenly distributed concentration of the sediment along flow height. In principle, fine particles should 414 be transported in continuous suspension, but if the current is oversaturated $(P_n *>1)$, a sedimentation 415 rate must be anyway allowed, although it is very small (tens of times lower than the case with coarser 416 particles, see Supporting file C and D). The settled fine ash remains attached to the ground and cannot 417 be re-eroded from the substrate (Gladstone et al., 1998). In summary: fine-grained pyroclastic density 418 currents, while leaving thin layers on the ground, travel further and possess a higher capacity of 419 impact over the territory. The impact potential is related to the presence of unbreathable hot ash 420 (Horwell and Baxter, 2006) and to the dynamic pressure of the flow $\frac{1}{2} \rho_{fl} u^2$, which in extreme cases 421 is able to destroy buildings (Valentine, 1998; Baxter et al., 2005; Neri et al., 2015). The distribution 422 of these impact parameters along flow runout is strongly influenced by the sedimentation rate. We 423 believe that the inclusion of the sedimentation rate in the numerical multiphase simulation codes, by 424 means of equations (5) and (6), would improve the ability to predict the hazard of pyroclastic density 425 currents on active volcanoes.

426 In order to effectively use our new model, it is important to have precise data on the physical 427 characteristics of the particles present in a current. Unfortunately, there are no theoretical models 428 giving a priori insights into the grain size, density and shape of the particulate mixture. Pyroclastic 429 deposits are the only record of the passage of pyroclastic density currents, and a prerequisite work in 430 the field is needed for getting information of the real particle population that feeds the flow. After a 431 detailed facies analysis that includes measurements of thickness and density of deposits, samples 432 collected from representative layers need to be processed in the laboratory for multicomponent grain-433 size analysis, including density and shape. On this regard, a word of caution must be spent on the 434 conditions that permit a proper application. Since our model is based on the concepts of sedimentation 435 from turbulent suspension and final traction at the bedload, a careful study of the deposit facies 436 architecture is needed in order to ascertain that such conditions are met. The occurrence of 437 asymmetrical bedforms, such as ripples and sand waves and of internal inclined lamination (see fig. 438 12) are features indicative of tractional processes at the bedload, which guarantee the application of 439 the model presented in this paper. However, pyroclastic density currents do not always behave as 440 turbulent suspensions, as it is the case of massive pyroclastic flows (Branney and Kokelaar, 2002), 441 or also the case of massive deposits from pyroclastic density currents found in proximal locations, 442 i.e. at the impact zone of the collapsing fountain (Sulpizio and Dellino, 2008; Sulpizio et al., 2014; 443 Dufek, 2016). An example of a metric thick, massive, structureless deposit formed by the impact of 444 the eruptive fountain feeding pyroclastic density currents of the Mercato eruption is shown, as an 445 example, on Fig. 14. The layer does not show any feature suggesting a particle selective transportation 446 in suspension or traction at the bedload. The model of sedimentation rate by turbulent suspension is 447 not applicable to this layer. In fact, at the impact, the particle volumetric concentration was so high 448 that particle-particle interaction played a stronger role than turbulent suspension upon deposition. 449 Judging from the experiments described in the present paper, it seems that the particulate mixture 450 issuing from the conduit and feeding the dense fountaining column did not undergo a grain size 451 selection upon the impact on the ground from where the "en mass" deposition of the massive layer 452 occurred. The grain size selection, in fact, started only after the development of the lateral turbulent 453 suspension current. It implies that, if thick, massive, structureless layers are formed by the collapse 454 of a natural eruptive column in the same way as in the experiments, their grain size, not having 455 underwent a selective process, can be taken as representative of the parent grain-size population 456 feeding the eruption. This outcome has important implication on the modelling of explosive 457 volcanism, since the parent grain-size population is one of the main parameters used for initializing 458 eruption simulations (Neri and Macedonio, 1996). Furthermore, concerning the modelling of grain 459 size of pyroclastic density currents, equation (6) allows the reconstruction of the grain size of the

460 material transported by turbulent suspension from the deposit or, vice-versa, the reconstruction of the 461 sedimented material grain size starting from that of the transported material. This information can be 462 used, in models, to predict the granulometric evolution of the particulate mixture during runout.

463 The sedimentation rate calculated for some pyroclastic density currents of Vesuvius and Campi 464 Flegrei falls within the range of experimental data, which is a guarantee of good scalability of the 465 model. Furthermore, the duration of the natural currents, as calculated by the model, is compatible 466 with the observations of historical eruptions, making us confident that the model allows a reasonable 467 reconstruction of the behaviour of natural currents. We expect that higher values of the sedimentation 468 rate will result when the model is applied to more powerful eruptions than those studied in this paper, 469 and a systematic investigation will allow acknowledging the true range that can be reached by 470 pyroclastic density currents. Probably there is an upper limit over which massive deposition takes 471 over suspension-sedimentation plus bedload-traction. Future investigations are required to determine 472 this limit.

473 As a conclusive remark, we suggest that the model proposed in this paper, as it is based on the general 474 laws that regulate the sedimentation of particulate material from turbulent suspension, can have 475 applicability beyond the study of pyroclastic density currents, for example to other geological density 476 currents such as turbidites.

477

478 References

Andrews, B. J., Manga, M. (2011), Effects of topography on pyroclastic density current runout and
formation of coignimbrites, Geology 39:1099-1102, doi:10.1130/G32226.1.

481

Andrews, B. J., Manga, M. (2012), Experimental study of turbulence, sedimentation, and
coignimbrite mass partitioning in dilute pyroclastic density currents, J. Volcanol. Geotherm. Res.
225-226:30-44, doi:10.1016/j.jvolgeores.2012.02.011.

- Baxter, P. J., Boyle, R., Cole, P., Neri, A., Spence, R., Zuccaro, G. (2005). The impact of
 pyroclastic surges on buildings at the eruption of the Soufrière Hills volcano, Montserrat, Bull.
 Volcanol. 67:292–313.
- 489
- Branney, M. J., Kokelaar, P. (2002). Pyroclastic Density Currents and the Sedimentation of
 Ignimbrites. Geological Society, London, Memoirs, 27.
- 492
- Brown, R.J., Branney, M.J. (2013). Internal flow variations and diachronous sedimentation within
 extensive, sustained, density stratified pyroclastic density currents down gentle slopes, as revealed by
 the internal architectures of ignimbrites in Tewnerife, Bulletin of Volcanology, 75:1-24,
 doi: 10.1007/s00445-013-0727-0.
- 497
- 498 Dade, W. B., Huppert, H. E. (1996). Emplacement of the Taupo ignimbrite by a dilute turbulent
 499 flow, Nature 381:509-512, doi:10.1038/381509a0.
- 500
- 501 Davis, J., C. (2002). Statistics and data analysis in Geology. Third Edition. John Wiley & Sons. New
 502 York. 638pp.
- 503
- 504 de Vita, S., Orsi, G., Civetta, L., Carandente, A., D'Antonio, M., Deino, A., di Cesare, T., Di
- 505 Vito, M. A., Fisher, R. V., Isaia, I., Marotta, E., Necco, A., Ort, M., Pappalardo, L., Piochi, M.,
- 506 Southon, J. (1999). The Agnano–Monte Spina eruption (4100 years BP) in the restless Campi Flegrei
- 507 caldera (Italy), J. Volcanol. Geotherm. Res. 91:269-301.
- 508
- 509 Dellino, P., Isaia, R., Veneruso, M. (2004). Turbulent boundary layer shear flows as an 510 approximation of base surges at Campi Flegrei (Southern Italy), J. Volcanol. Geotherm. Res. 511 133:211-228.

513 Dellino, P., Mele, D., Bonasia, R., Braia, G., La Volpe, L., Sulpizio, R. (2005). The analysis of the
514 influence of pumice shape on its terminal velocity, Geophys. Res. Lett. 32:L21306.
515 doi:10.1029/2005GL023954.
516
517 Dellino, P., Zimanowski, B., Büttner, R., La Volpe, L., Sulpizio, R. (2007). Large-scale
518 experiments on the mechanics of pyroclastic flows: Design, engineering, and first results, J. Geophys.

519 Res. 112:B04202. doi:10.1029/2006JB004313.

520

521 Dellino, P., Mele, D., Sulpizio, R., La Volpe, L., Braia, G. (2008). A method for the calculation of
522 the impact parameters of dilute pyroclastic density currents based on deposit particle characteristics,
523 J. Geophys. Res. 113:B07206. doi:10.1029/2007B005365.

524

Dellino, P., Dioguardi, F., Zimanowski, B., Büttner, R., Mele, D., La Volpe, L., Sulpizio, R.,
Doronzo, D. M., Sonder, I., Bonasia, R., Calvari, S., Marotta, E. (2010a). Conduit flow
experiments help constraining the regime of explosive eruptions, J. Geophys. Res. 115:B04204,
doi:10.1029/2009JB006781.

529

Dellino, P., Büttner, R., Dioguardi, F., Doronzo, D. M., La Volpe, L., Mele, D., Sonder, I.,
Sulpizio, R., Zimanowski, B. (2010b). Experimental evidence links volcanic particle characteristics
to pyroclastic flow hazard, Earth Planet. Sc. Lett. 295:314-320. doi:10.1016/j.epsl.2010.04.022.

533

534 Dellino, P., Dioguardi, F., Mele, D., D'Addabbo, M., Zimanowski, B., Büttner, R., Doronzo, D.

535 M., Sonder, I., Sulpizio, R., Dürig, T., La Volpe, L. (2014). Volcanic jets, plumes, and collapsing

536 fountains: evidence from large-scale experiments, with particular emphasis on the entrainment rate,

537 Bull. Volcanol. 76:834, doi:10.1007/s00445-014-0834-6.

539	Dioguardi, F., Dellino, P. (2014). PYFLOW: A computer code for the calculation of the impact
540	parameters of Dilute Pyroclastic Density Currents (DPDC) based on field data, Comput. Geosci.
541	66:200-210, doi:1 0.1016/j.cageo.2014.01.013.
542	
543	Dioguardi, F., Mele, D. (2015). A new shape dependent drag correlation formula for non-spherical
544	rough particles. Experiments and results, Powder Technol. 277:222-230,
545	doi:10.1016/j.powtec.2015.02.062.
546	
547	Doronzo, D.M., Dellino, P., Sulpizio, R., Lucchi, F. (2017). Merging field mapping and numerical
548	simulation to interpret the lithofacies variations from unsteady pyroclastic density currents on uneven
549	terrain: The case of La Fossa di Vulcano (Aeolian Islands, Italy), J. Volcanol. Geotherm. Res. 330:36-
550	42.
551	
552	Dufek, J. (2016). The Fluid Mechanics of Pyroclastic Density Currents, Annu. Rev. Fluid Mech.
553	48:459–85, doi: 10.1146/annurev-fluid-122414-034252.
554	
555	Gladstone, C., Phillips, J. C., Sparks, R. S. J. (1998). Experiments on bidisperse, constant-volume
556	gravity currents: propagation and sediment deposition, Sedimentology 45:833-843,
557	doi:10.1046/j.1365-3091.1998.00189.x.
558	
559	Horwell, C. J., Baxter, P. (2006). The respiratory health hazards of volcanic ash: A review for
560	volcanic risk mitigation, Bull. Volcanol. 69:1-24, doi:10.1007/s00445-006-0052-y.

562 Kneller, B., Buckee, C. (2000). The structure and fluid mechanics of turbidity currents: a review of
563 some recent studies and their geological implications, Sedimentology 47(Suppl. 1):62-94,
564 doi:10.1046/j.1365-3091.2000.047s1062.x.

565

Lube, G., Cronin, S. J., Platz, T., Freundt, A., Procter, J. N., Henderson, C., Sheridan, M. F.
(2007). Flow and deposition of pyroclastic granular flows: A type example from the 1975 Ngauruhoe
eruption, New Zealand, J. Volcanol. Geotherm. Res. 161(3):165-186,
doi:10.1016/j.jvolgeores.2006.12.003.

570

Manville, A., Segschneider, B., Newton, E., White, J.D.L., Houghton, B.F., Wilson, C.J.N.
(2009). Environmental impact of the 1.8 ka Taupo eruption, New Zealand: Landscape responses to a
large-scale explosive rhyolite eruption. Sedimentary Geology. 220:318-336,
doi:10.1016/j.sedgeo.2009.04.017.

575

Mele, D., Sulpizio, R., Dellino, P., La Volpe, L. (2011). Stratigraphy and eruptive dynamics of a
pulsanting Plinian eruption of Somma-Vesuvius: the Pomici di Mercato (8900 years B.P.), Bull.
Volcanol. 73:257-278, doi: 10.1007/s00445-010-0407-2.

579

Mele, D., Dioguardi, F., Dellino, P., Isaia, R., Sulpizio, R., Braia, G. (2015). Hazard of pyroclastic
density currents at the Campi Flegrei Caldera (Southern Italy) as deduced from the combined use of
face architecture, physical modeling and statistics of the impact parameters, J. Volcanol. Geotherm.
Res. 299:35-53, doi: 10.1016/j.jvolgeores.2015.04.002.

584

585 Middleton, G. V., Southard, J. B. (1984). Mechanics of Sediment Movement, 2nd ed., Society of
586 Economic Paleonologists and Mineralogists, Tulsa, OK, 401 pp.

588	Neri, A., Macedonio, G. (1996). Numerical simulation of collapsing volcanic columns with particles
589	of two sizes, Journal of Geophysical Research, 101:8153-8174.

- Neri, A., Esposti Ongaro, T., Voight, B., Widiwijayanti, C. (2015). Pyroclastic density currents
 hazards and risk. In: Volcanic Hazard, Risks and Disasters, Eds.: Shroder, J. F., Papale, P., Elsevier.
- 594 **Pope, S. B.** (2000). Turbulent flows. Cambridge University Press, 771 pp.

595

Roche, O. (2015). Nature and velocity of pyroclastic density currents inferred from models of
entrainment of substrate lithic clasts, Earth Planet. Sci. Lett. 418:115-125,
doi:10.1016/j.epsl.2015.03.001.

599

Rouse, H. (1939). An analysis of sediment transportation in the light of fluid turbulence, in Soil
Conservation Services Report No. SCS-TP-25, USDA, Washington, D.C.

- 603 Schlichting, H., Gersten, K. (2000). Boundary-Layer Theory, Springer, Berlin, 801 pp.
 604
- 605 Sparks, R. S. J., Bursik, M. I., Carey, S. N., Gilbert, J. S., Glaze, L. S., Sigurdsson, H., Woods,
 606 A. W. (1997). Volcanic Plumes, Wiley-Blackwell.
- 607
- Sulpizio, R., Dellino, P. (2008). Sedimentology, depositional mechanisms and pulsating behavior of
 pyroclastic density currents, In: Martì, J., Gottsman, J. (Eds.) Calderas Volcanism: Analysis,
 Modelling and Response, vol. 10, Developments in Volcanology, Elsevier, Amsterdam, pp. 57-96.
- 611

612	Sulpizio, R., Dellino, P., Doronzo, D. M., Sarocchi, D. (2014). Pyroclastic density currents: state
613	of the art and perspectives, J. Volcanol. Geotherm. Res. 283:36-65,
614	doi:10.1016/j.jvolgeores.2014.06.014.
615	
616	Valentine, G. A. (1987). Stratified flow in pyroclastic surges, Bull. Volcanol. 49:616-630.
617	
618	Valentine, G.A., Doronzo, D.M., Dellino, P., de Tullio, M.D. (2011). Effects of volcano profile on
619	diluite pyroclastic density currents: Numerical simulations, Geology 39:947-950,
620	doi:10.1130/G31936.1.
621	
622	Wilson, C. J. N., Houghton, B. F., Kampt, P. J. J., McWilliamst, M. O. (1995). An exceptionally
623	widespread ignimbrite with implications for pyroclastic flow emplacement, Nature 378:605-607,
624	doi:10.1038/378605a0.
625	
626	
627	
628	Caption of figures
629 630 631 632 633	Fig. 1. Grain-size distribution of the material used for experiments. A: multicomponent grain-size distribution of the coarse material coming from the Veusvius composition. The relative fractions of components are shown. The xx symbol means crystals. B: grain-size distribution of the fine glassy material coming from the Campi Flegrei composition.
634 635 636	Fig. 2. Skecth design of the experimental apparatus with description of the main parts. Modified after Dellino et al., 2017.
637 638 639 640 641 642	Fig. 3. Display mount showing phases of the experiment and associated deposits. A: formation of the dense gas-particle foutain at the conduit exit. B: Collapse of the fountain and impact on the ground. C: development of the fully turbulent current. D: Massive deposit formed at the impact area where the flow is not extablished yet. Deposit with tractional features of the type of ripples formed by the fully turbulent suspension current. E: Fan shape distribution of the deposits.
643 644 645	Fig. 4. Grain-size distribution of the massive layer formed at the impact of the experimental fountain. A: grain size of a "coarse" run. B: grain size of a "fine" run.

647 Fig. 5. Graph showing the correlation between the ratio of the particle volumetric concentration of 648 the transported material, C_i , and the proportion of the material sedimented from turbulent suspension, v_i of the particle size classes as a function of the Rouse number of the size class P_{ni} . For 649 650 comparison, data from a coarse run and data from a fine run are represented, together with the respective correlation coefficient, regression equation and normalized Rouse number Pn*. 651 652 653 Fig. 6. Graph showing the correlation between the ratio of the particle volumetric concentration of 654 the transported material, C_i , and the proportion of the material sedimented from turbulent 655 suspension, γ_i of the particle size classes as a function of the ratio of Particle Rouse number of the 656 size fraction P_{ni} and normalized Rouse number Pn*. Data of all the components and size classes of 657 all experiments are included. The correlation coefficient and regression equation are inset. 658 659 Fig. 7. Graph showing the correlation between the measured sedimentation rate and the 660 sedimentation rate calculated by means of γ_{proxy_i} . The regression equation and correlation coefficient are inset. 661 662 Fig. 8. Graph showing the correlation between the measured sedimentation rate and the 663 sedimentation rate calculated by means of γ_{true_i} . The regression equation and correlation 664 665 coefficient are inset. 666 Fig. 9. Graph showing the correlation between the measured sedimentation rate and the 667 sedimentation rate calculated by means of equation (5). The regression equation and correlation 668 coefficient are inset. 669 670 671 Fig. 10. Comparison between the grain-size distribution of the transported material and that of the 672 sedimented material. A: Coarse composition coming from Vesuvius. B: fine composition coming 673 from Campi Flegrei. 674 675 Fig. 11. Graph showing the variation of the median size of the grain-size distribution of samples as 676 a function of distance from the impact location for an experimental run fed with corse material 677 (dots) and one with fine material (triangles). D is maximum distance, d is distance from the impact. 678 679 Fig. 12. Photos showing the facies of deposits used for the application of the model of the 680 sedimentation rate. A: layer of the Mercato eruption at Vesuvius showing tractional structures. B: 681 layer of the Agnano Monte Spina eruption showing inclined laminae. 682 683 Fig. 13. Multicomponent grain-size distribution of layers used for the application of the model of 684 the sedimentation rate. A: multicomponent grain-size distribution of the layer from the Mercato 685 eruption at Vesuvius. B: multicomponent grain-size distribution of the layer from the Agnano 686 Monte Spina eruption at Campi Flegrei. 687 688 Fig. 14. Photo showing a massive, structureless layer of the Mercato eruption formed at the impact 689 of a collapsing eruptive fountain.